Tribology International 179 (2023) 108155

Contents lists available at ScienceDirect

Tribology International

journal homepage: www.elsevier.com/locate/triboint

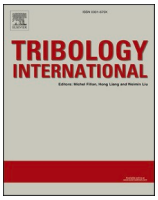

Variable pressure scuffing of a flake graphite cast iron diesel cylinder liner

J.C. Walker [a,*], Z. Barnes [a], A. Shehata [a], P. Jiang [a], T.J. Kamps [b]

[a] National Centre for Advanced Tribology, University of Southampton, UK
[b] Advanced Materials Characterisation, NPL, UK

ARTICLE INFO

Keywords:
Scuffing
Cast iron
Piston ring
Glaze
Oxidative

ABSTRACT

A novel scuffing methodology was developed utilising variable specimen geometry to replicate numerically modelled top compression ring contact pressures (4–62 MPa) from a 12.8-litre heavy duty diesel engine as a function of stroke position. Scuffing of grade 250 cast iron was induced by reciprocating sliding (TE77) against a drip lubricated (PAO4) 52100 rectangular contact operating at 15 Hz and 311 N normal load by incrementing the temperature at 4°C per minute until a sharp rise in friction coefficient was observed. Scuffing initiation temperature was insensitive to dynamic contact pressure. Formation of an oxide 'glaze' layer resulted in friction coefficients as low as 0.03 prior to severe scuffing.

1. Introduction

The need to reduce emissions and improve fuel economy continues to drive the trend towards lower viscosity lubricants for off highway heavy duty diesel powertrains. Whilst this approach is effective for reducing viscous shear losses in the fluid film lubrication regime, it can also increase the propensity for film instability during demanding duty cycles, raising the incidences of asperity contact which can cumulatively contribute to scuffing at the ring – liner interface. Scuffing in combustion engines can be caused by various factors (e.g. insufficient or interrupted cooling, extensive heat generation, high rpm for extended periods) and is characterised by macroscopically observable directional modification of the surface morphology [1]. In many cases is sufficiently severe that oil consumption and blow-by increase to an unacceptable level that can result in piston seizure [2]. Screening ring liner material pairs for scuffing resistance is challenging, not least because of both the subtle nature of mild scuffing initiation but also the rapid progression to severe failure [3–9].

Laboratory based methodologies to replicate reciprocating engine scuffing are based around achieving failure through lubricant starvation or degradation through a net energy input into the contact by increasing test temperature or contact load [7,8,10–15]. Cylindrical Hertzian line contacts are often utilised to represent the ring-liner interface [7,8,10,11] as repeatable alignment can be achieved with relative ease. This is an effective approach for comparing different materials when test conditions are identical. However it suffers from a drawback in terms of the dynamic contact pressure which is difficult to control as it continually changes as both a function of test duration (due to wear of the cylinder) but also any increments in load used to facilitate scuffing. As such, it becomes necessary to control the contact pressure by minimising changes to the contact area during scuffing tests. Replicating the dynamic load profile that exists between the ring and liner during the engine compression and expansion stroke in such experiments can be further challenging due to the dynamic force response required at representative test frequencies. Attempts have been made in this regard using profiled cam-follower arrangements to either steadily increase the load profile along the stroke [16] or provide a shock load at the reversal position [15]. An alternative methodology that varies the contact pressure by applying a constant normal load and altering the specimen geometry from a rectangular to triangular wedge geometry [17] is an different approach that could be a more realistic representation of the dynamic load variation experienced by the ring-liner contact. This paper develops this idea by numerically simulating the expected dynamic load profile of a top compression ring from a typical off highway heavy duty diesel engine. The representative profile is translated directly to a test coupon of the engine liner material. As a constant load is required to maintain the specified dynamic contact pressure, scuffing was induced through an externally heated temperature ramp approach.

2. Methodology

2.1. Engine modelling

In order to replicate the dynamic contact pressures experienced

* Corresponding author.
E-mail address: j.walker@soton.ac.uk (J.C. Walker).

https://doi.org/10.1016/j.triboint.2022.108155
Received 21 September 2022; Received in revised form 30 November 2022; Accepted 2 December 2022
Available online 5 December 2022

between the top compression ring and the cylinder liner wall during scuffing of a heavy-duty diesel engine numerical modelling of the contact using Ricardo RINKPAK software was undertaken. The software is an integrated numerical solver that allows ring forces to be determined as a function of crank angle by modelling the hydrodynamic behaviour, inertia force, boundary contact, gas pressure, and ring stiffness. The hydrodynamic lubrication effects were solved using through a solution to the Navier-Stokes equation to predict the shape and extent of the scraped oil film layer based on the equilibrium between oil inertia and the shear stress. A Reynolds and Jakobsson-Floberg-Olsson (JFO) model was used to determine the hydrodynamic boundary conditions between the ring and liner whilst asperity properties in the boundary lubrication regime were determined from through a summit height corrected Greenwood-Williamson-Tripp derivation, based on a Hertzian analysis [18–20]. A 12.8 litre 470 hp inline 6 direct injection diesel using a SAE10W lubricant was selected as the model engine, with key engine geometries and parameters used in the numerical study listed in the Appendix. As the study was interested in the onset of scuffing, the RINGPAK simulation was run at a high constant engine velocity of 2000 rpm, which produced a peak in-cylinder pressure of 125 bar, Fig. 1, consistent with published data from similar heavy duty diesel engines [21,22].

The top compression ring radial load profile generally follows the in-cylinder pressure profile [22] as the gas pressure and ring inertia in the first piston groove is exerted on the ring, Fig. 2, peaking at 16,273 N at a crank angle of 7.7° and consistent with similar studies [23]. The ring reaction forces depend on a number of factors including the ring stiffness and groove friction, however the peak asperity contact force in the boundary condition was calculated to be 4975 N, similar to previous studies that attempt to replicate tribological contacts of heavy duty diesel top compression rings in the laboratory [24].

Due to ring dynamics associated with the crank geometry, peak contact pressures would necessarily be higher on the thrust side of the piston. This made it necessary to resolve the ring contact pressures as a function of both the crank position and the axial ring width location, Fig. 3. It was observed that peak instantaneous contact pressure on the top compression ring rose to as high as 70.8 MPa in the vicinity just after the TDC position and was very localised on the ring axial position. This was consistent with predicted peak hydrodynamic ring pressures of other diesel engine studies at a similar crank angle position [25–28]. The contact pressure during the remainder of the stroke was an average of 7.9 MPa.

2.2. Specimen geometry

The peak and minimum contact pressures determined from the simulation results in Fig. 3 were utilised to guide the manufacture of two specimen geometries for scuffing studies: a) A planar constant pressure flat plate geometry and b) a curved variable pressure geometry, as shown in Fig. 4. The dynamic pressure variable geometry was based upon the radial ring force curve in Fig. 3 which exhibited a continuous transition in contact pressure along the stroke. The key parameter for designing the specific coupon geometry was the rectangular contact area of the counter surface, representing a square face top compression ring contact, as this determined the nominal contact pressure applied at a specific stroke position for a given constant normal load. A contact area of 1.97 × 20 mm was chosen as a balance between the geometrical constraints imposed by the reciprocating test equipment utilised in this study (discussed below), the dimensional width of the model engine top compression ring (3 mm) and the challenges associated with conformal surface alignment for rectangular contact widths below 1.5 mm. The counter surface was a 6 mm diameter 52100 through hardened bainitic steel roller bearing element of 20 mm length (Atlas Bearings, UK). This was flat lapped using a Kemet 25 cast iron plate with 25 μm diamond slurry until a 1.97 mm wide flat contact surface had been achieved, Fig. 5a), with an average surface roughness, R_a, of 2.12 ± 0.14 μm. The test configuration schematically illustrated in Fig. 4 shows a transparent lapped 52100 counter surface, with the rectangular contact area visible at the bottom surface.

The geometry of the specimen was designed such that the test could operate at a constant normal load of 311 N, with variations in contact pressure being achieved by the change in contact width between the counter surface and the curved specimen geometry. The curve was designed such that when the full area of the counter surface was in contact with the plate specimen, a contact pressure of 7.9 MPa would be applied. As the counter surface moved along the curved surface towards the narrowest point, the contact pressure would increase to a predicted maximum value of 61.7 MPa, Fig. 6. These values were calculated by dividing the normal load (311 N) with the integrated contact area of the counter surface at each stroke position using the trapezium (Newton-Raphson) method. The reversal position of the leading edge of the counter surface at the narrow end of the curve was 1.49 mm from the curve termination and simulated the end of the compression cycle prior to TDC. The constant pressure sample was designed as a flat planar surface with a constant nominal contact pressure of 7.9 MPa along the entire stroke length.

Flat plate specimens of 58×38×4 mm were manufactured from Grade 250 flake graphite grey cast iron (West Yorkshire Steel, UK). The curve profile was introduced using a CNC mill to reduce the thickness dimension by 1 mm at the curve boundary with chamfered edges. The width of the contact area at the narrowest position of the curve was 2.23 mm to achieve a maximum contact pressure of 61.7 MPa. In order

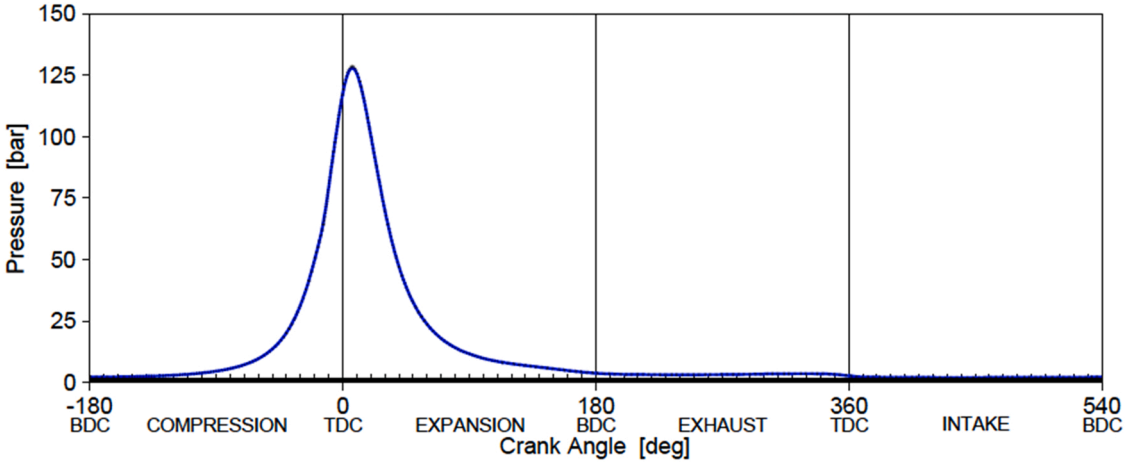

Fig. 1. Simulated in-cylinder pressure as a function of crank angle.

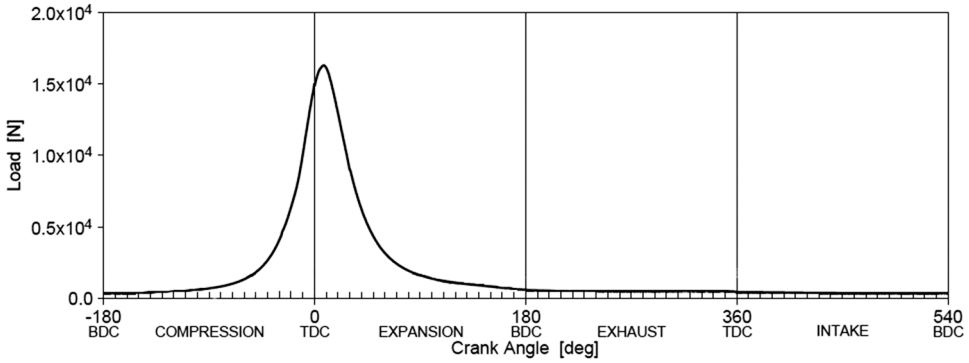

Fig. 2. Simulated radial load applied to top compression ring as a function of crank angle.

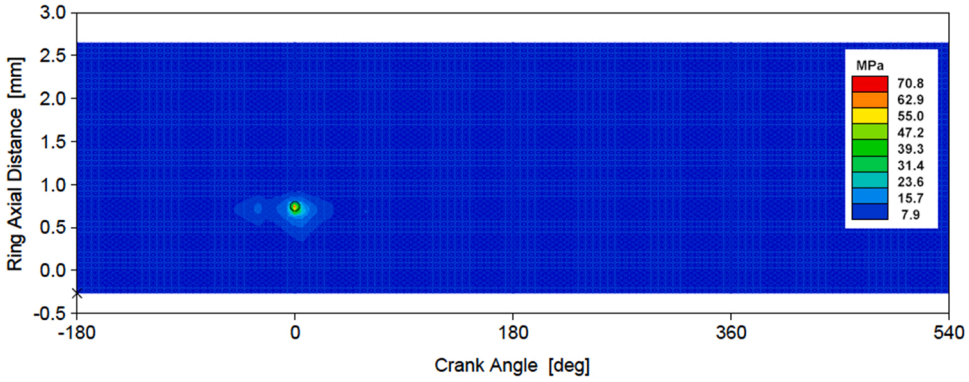

Fig. 3. Simulated contact pressure distribution on top compression ring as a function of crank angle.

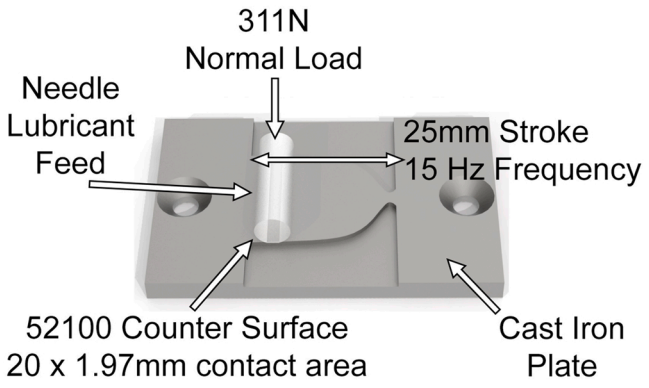

Fig. 4. Variable pressure specimen geometry and test configuration.

to replicate the honing pattern that would be present on a cylindrical liner, each plate specimen was ground at 45° to the reciprocating direction to an average value of 1.04 ± 0.09 μm Ra, as shown in Fig. 5b).

2.3. Scuffing methodology

A Phoenix Tribology TE77 high frequency reciprocating tribometer was used to perform the variable pressure scuffing tests in a rectangular area contact configuration. An unformulated synthetic polyalfaolefin (Spectrasyn 4) was drip fed at a rate of 0.5 ml/hr via a fine bore needle to the low-pressure end of the plate specimen. The rectangular area of the counter surface was aligned on the lubricated plate specimen by loading the contact to the test load of 311 N without constraining movement. This allowed the back face of the counter surface to pivot on cylindrical pin located in the reciprocating head assembly and thus self-align before being clamped tight. To confirm the contact was aligned, the counter surface was oscillated at a frequency of 15 Hz, stroke length of 25 mm at a 5 N normal load before increasing to the constant test load of 311 N. The presence of a symmetrical friction force and contact potential for both stroke directions confirmed conformal counter surface alignment. In order to facilitate scuffing, the temperature of the specimen was increased at a rate of 4 °C/min (measured with a class 1 K-type thermocouple) until severe scuffing was observed by a rapid increase in the average coefficient of friction [7,8,10,11]. The test was immediately terminated upon this observation and the specimens allowed to cool prior to being cleaned in petroleum ether. Tests were repeated twice to ensure repeatable results. Both constant and variable pressure contact surfaces were examined using a combination of non-contact optical profilometry (Alicona Infinitefocus), Scanning Electron Microscopy (SEM – Jeol 7200 F) and Energy Dispersive X-ray Spectroscopy (EDX – Oxford Instruments).

3. Results

3.1. Friction behaviour

The average coefficient of friction for both constant and variable pressure specimens was calculated as a r.m.s average value across the entire stroke length and plotted as a function of specimen temperature in Fig. 7. Tests commenced sliding between 22 and 34 °C although this was not thought to have influenced the scuffing behaviour. The high coefficient of friction values observed at the beginning of the test were recorded prior to sliding when application of the normal load through zero force causes a momentary infinite coefficient. Sliding commenced at 5 N load to confirm conformal alignment prior to ramping to 311 N normal load and initiation of the temperature ramp. It was observed that beyond 70 °C, the constant pressure specimens generally exhibited a slightly higher average coefficient of friction compared to the variable

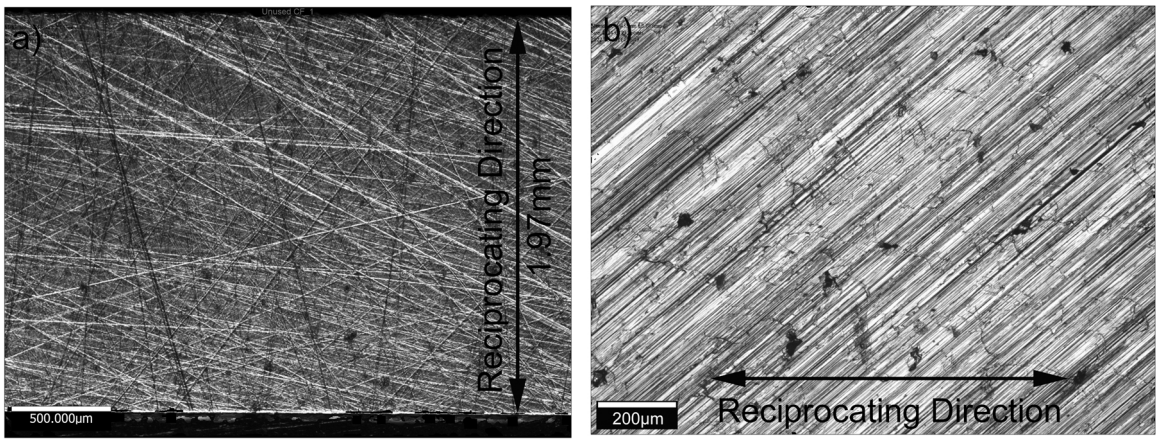

Fig. 5. Optical microscopy images of a) lapped 52100 counter surface with 20 × 1.97 mm contact area and b) grade 250 cast iron ground at 45° to counter surface reciprocating direction.

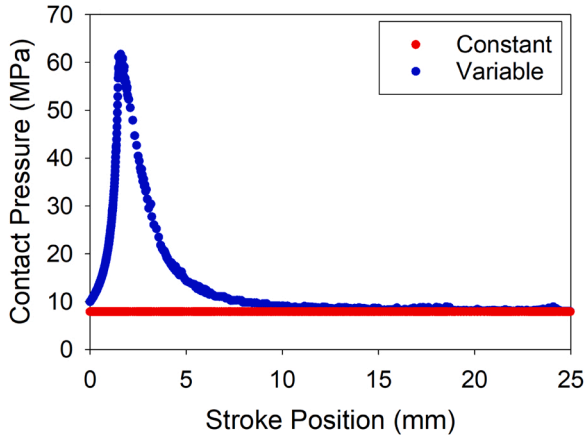

Fig. 6. Nominal contact pressure vs stroke position for constant and variable pressure surfaces.

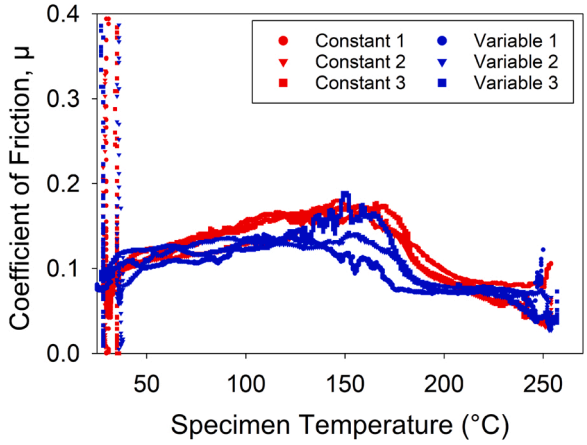

Fig. 7. Coefficient of friction as a function of specimen temperature.

pressure specimens up to 200 °C, with the exception of the Variable 3 test that briefly exhibited similar values around 150 °C.

Both types of specimen geometry experienced the same general trend as the temperature was incremented. After 150 °C a gradual decrease in the average coefficient of friction was observed for both specimens prior to severe scuffing initiation at 252 ± 6 °C for the variable pressure specimen and 249 ± 6 °C for the constant pressure specimen. A high contact potential was observed between the sliding surfaces during the early phase of the test between at 60–72 °C indicated the presence of a lubricating film for both specimen types as shown by the instantaneous friction force and contact potential graphs for ten strokes in Fig. 8. The magnitude of the contact potential appeared higher for constant pressure specimens, Fig. 8g), suggesting the lack of any discontinuity in geometry perhaps facilitated a consistent lubricating film. The variable pressure specimens experienced a consistent drop in the contact potential around the narrowest contact point (at the 10 mm stroke position), Fig. 8a), c) and e), although interestingly this drop was asymmetrical and dependent on the direction of sliding. As the counter surface approached the constriction (moving in the positive direction), the contact potential dropped to a minimum value at a stroke position of 7.6 mm, in advance of the narrowest point, before recovering to a higher value as the reversal position was reached. After reversal, a lubricating film was unable to form until the 9.8 mm position had been passed (moving in the negative direction), with the absolute magnitude of the contact potential always less compared to the reciprocal direction.

As the temperature of the test increased, it was observed that the contact potential across the stroke reduced towards zero indicating collapse of the lubricating film and a corresponding transition to the boundary lubrication regime occurred for the constant pressure specimen at a temperature of 100 ± 27 °C. This was in contrast to the variable pressure specimen which continued until 136 ± 14°C before this transition was observed and may explain the slightly higher magnitude of average friction coefficient observed in Fig. 7.

At a test temperature of above 200 °C, all specimen geometries had experienced a decrease in their average coefficient of friction to just below 0.1. Fig. 8b), d), f) and h) shows the instantaneous friction force data for specimens immediately prior to the transition to severe scuffing. It was observed that an increase in the contact potential signal for the variable pressure specimens was commensurate with a decrease in the friction force position immediately prior to failure, yet the position was not necessarily located at the region of highest contact pressure. The constant pressure surfaces did not exhibit a change in contact potential prior to failure, Fig. 8h).

3.2. Surface analysis

Optical microscopy images from typical test plates and mating counter surfaces were shown in Fig. 9. The variable pressure test 1 and 2 had been allowed to continue for a couple of seconds beyond severe scuffing initiation which had resulted in severe adhesive wear, Fig. 9a), however this was not always observed in the region of highest contact pressure Fig. 9b) and c). This region was however characterised by the disappearance of the ground lay, surface cracks and the formation of a

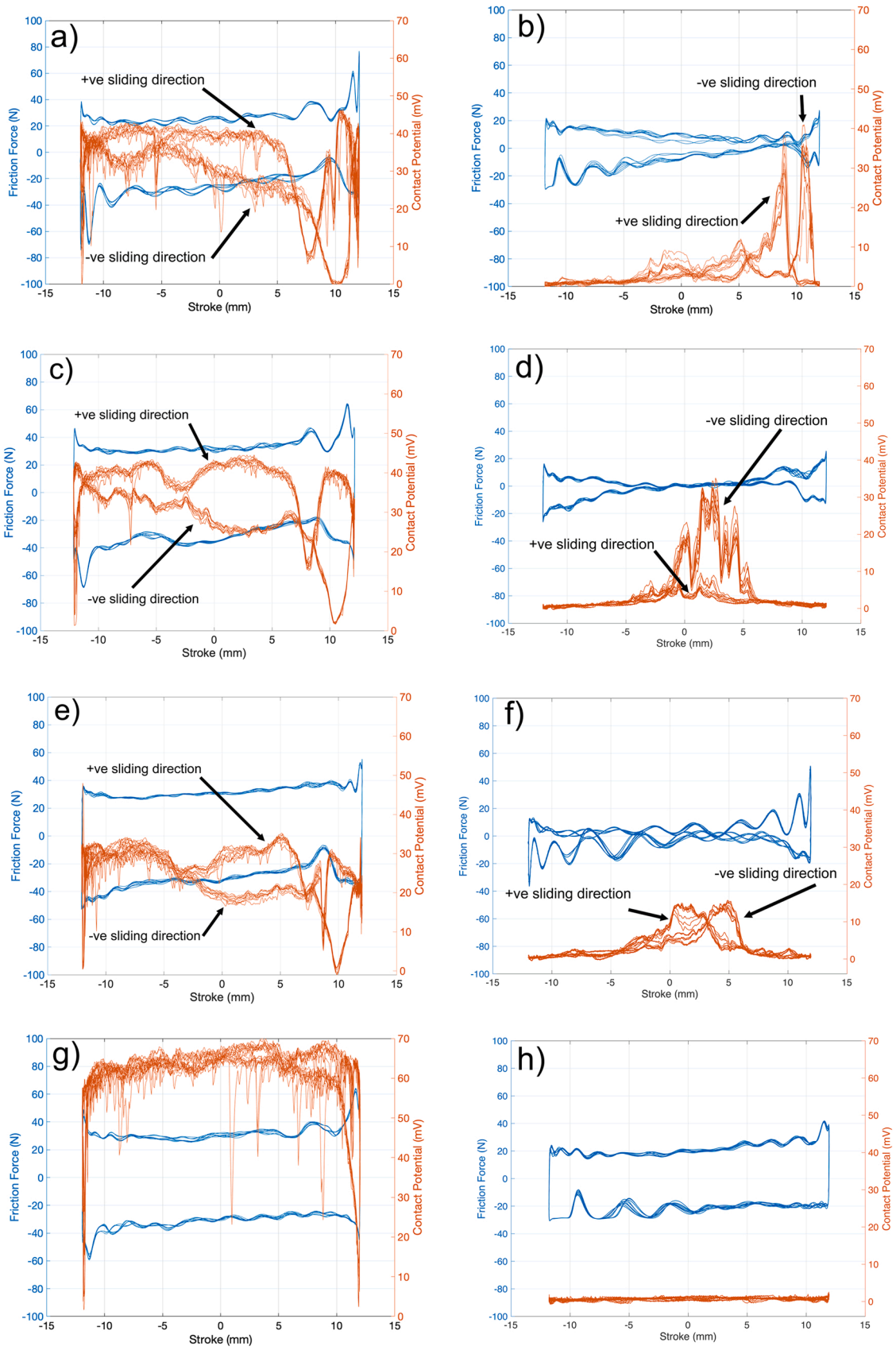

Fig. 8. Friction force and contact potential as a function of stroke position: Variable pressure test 1 at a) 60°C and b) 247°C; Variable pressure test 2 at c) 72°C and d) 253°C; Variable pressure test 3 at e) 68°C and f) 251 °C; Constant pressure test 1 at g) 60°C and h) 249°C.

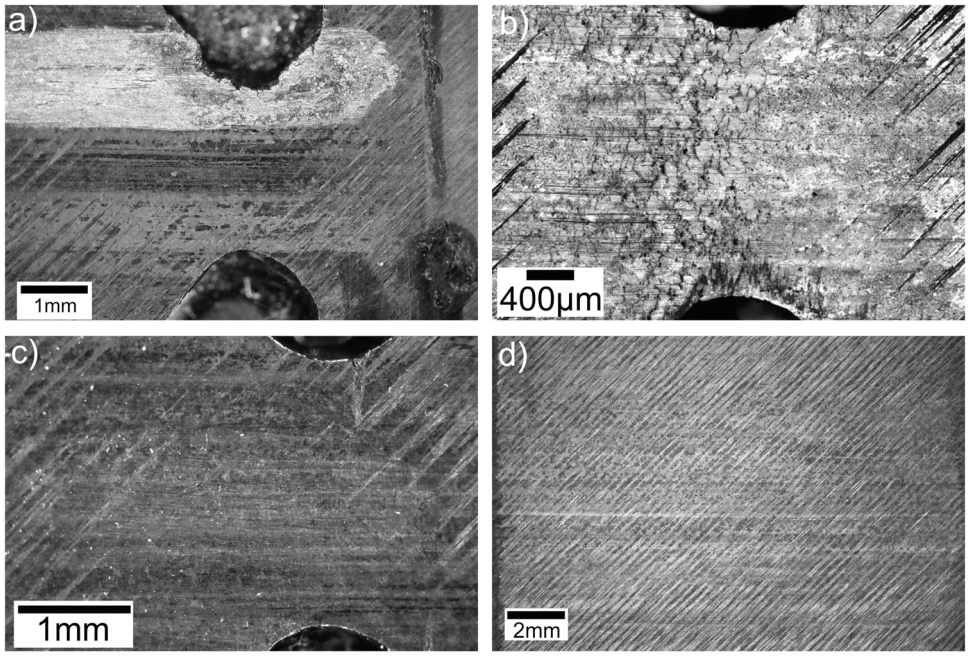

Fig. 9. Optical microscopy images of scuffed surfaces: a) Variable pressure test 1; b) Variable pressure test 2; c) Variable pressure test 3; d) Constant pressure test 1.

darker contrast surface phase aligned to the reciprocating direction, with an associated drop in average surface roughness (R_a) to a value of 0.35 ± 0.09 μm. The same observations were made on the constant pressure specimen, Fig. 9a), although not concentrated at a particular location, but evenly distributed across the worn surface, with a drop in average surface roughness (R_a) to value of 0.37 ± 0.12 μm. The counter surfaces all exhibited conformal contact with no evidence of edge loading, important for achieving the require dynamic pressure distribution. The average surface roughness of the counter surface measured after each test and away from any adhesive transfer material was found to be 2.14 ± 0.45 μm and 1.30 ± 0.46 μm for the constant and variable pressure specimens, respectively.

In order to investigate the darker phase present on the surfaces of both specimens immediately prior to severe scuffing, scanning electron microscopy with energy dispersive X-ray analysis of the variable pressure specimen test 1 surface at the position of highest contact pressure was shown in Fig. 10. It was observed at high magnification that the wear tracks parallel to the sliding direction in the smooth region of the variable pressure specimen appeared to be composed of a compacted surface layer of nanometre sized wear particles. The layer was not comprehensive but appeared to have been discontinuous worn away in places. Surface chemical EDX analysis, Fig. 10 b), suggested that the layer was primarily composed of an oxide of iron, with the presence of Si and C also noted.

4. Discussion

4.1. Asymmetric friction behaviour

The counter surface would replenish lubricant from the needle drip feed at the low pressure stroke reversal position. As the counter surface on the variable pressure specimen moved in the positive stroke direction, the continuous decrease in contact area corresponded to a decrease in the contact potential signal, Fig. 8a), c) and e), to a minimal value observed at 7.6 mm stroke position, 2.4 mm in advance of the counter surface beginning to transition the narrowest point of the contact area. The passing of the counter surface over the limit of the curved geometry led to a steady reduction of the established film due to lubricant edge effects [29,30]. The increase in contact potential beyond this position as the counter surface entered the narrow constriction indicated that the increase in contact pressure was effective at re-establishing the fluid film in this region despite the continuous decrease in velocity. The fact that this effect was not observed after reversal, sliding in the opposite direction, could be attributed to a squeeze film effect where friction behaviour is often asymmetrical for a reciprocating contact depending on whether the counter surface is accelerating or decelerating [31,32].

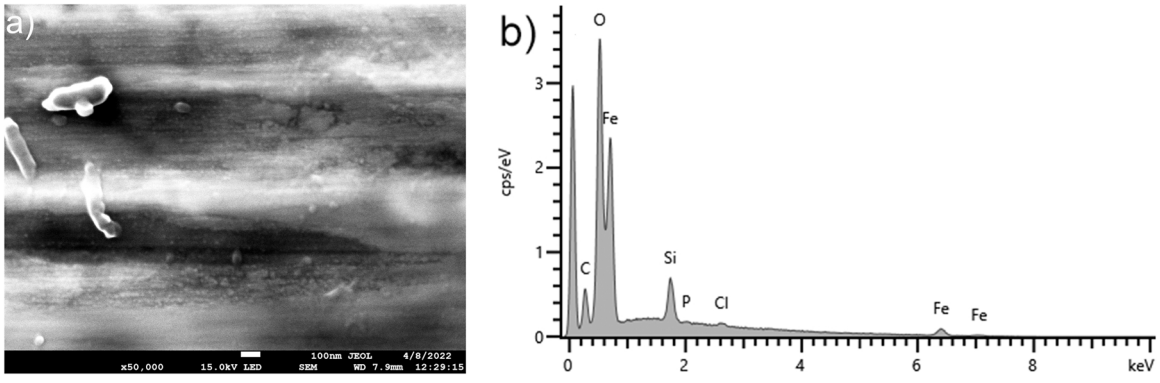

Fig. 10. Secondary electron image (a) and EDX spectrum (b) of scuffing initiation region on the variable pressure specimen.

The fact that the contact potential was always lower in magnitude in the negative sliding direction suggested a lack of available fluid to replenish the contact after the constricted position, until the lubricant was replenished at the low pressure reversal position, similar to that experienced in a ring pack in a combustion engine.

The marginally higher average coefficient of friction observed for the constant pressure specimen, Fig. 7, was attributed to the collapse of the lubricant film and transition at a lower temperature (100 ± 27 °C) compared to the variable pressure specimen (136 ± 14 °C). A decrease in lubricant viscosity and transition from fluid film to boundary conditions as the test temperature increased would necessarily increase the average coefficient of friction as the test progressed. The reason that the constant pressure specimen experienced this transition earlier in the test could be attributed to the lower contact pressure experienced over the entire stroke. As the variable pressure specimen experienced higher contact pressures, this would cause an enhanced running-in period that would condition the variable pressure surface more than the constant pressure surface, removing more material through wear and ensuring a more conformal surface that would prolong the transition from mixed to boundary lubrication. This was confirmed by the average surface roughness measurements of the counter surfaces which were lower for the variable pressure tests.

4.2. Surface oxide

Despite the small difference in absolute magnitude, both specimens began to experience a decrease in the average coefficient of friction around a test temperature of 150 °C, which has been suggested as the critical temperature associated with desorption of polar molecules within the lubricant [33,34]. The increase in contact potential signal prior to severe scuffing suggested that under boundary lubrication conditions, surface oxidation of the iron may be initiating at temperatures above 150 °C, resulting in the build-up of a low friction surface species, an observation consistent from multiple studies on oxidational wear [35] and supported by the SEM and EDX results in Fig. 10.

Immediately prior to the onset of severe scuffing, a further drop in the average coefficient of friction to values as low as 0.03 was observed before a rapid increase indicated scuffing initiation. The instantaneous friction force and contact potential prior to severe scuffing on the variable pressure specimens, Fig. 8b), d) and f) indicated how the localised build-up of an oxide layer led to an increase in the contact potential signal [35] in the region of the lowest friction force. Interestingly, this effect was not necessarily confined to the region of highest contact pressure, suggesting that the position of scuffing initiation was not necessarily dependent upon the location of highest contact pressure associated with the beginning of the expansion stroke in an engine. The contact potential exhibited stroke dependent asymmetry for the variable pressure specimens prior to scuffing initiation, Fig. 8 b_, d) and f) and was observed to increase in the positive half of the stroke position. This suggested that the oxide species formed in the region of highest contact pressure (as shown in Figs. 9 and 10) through an increase in asperity flash temperatures [37] was prone to rupture and redistribution. This asymmetry caused by variable pressure which was not observed in the constant pressure sample could possibly indicate the dynamic nature of the oxide glaze layer, being continually removed and reformed as a function of stroke position. This suggested that surface oxide film was synergistic to both contact pressure but also the relative velocity, a concept noted in the literature others as being significant in terms of scuffing initiation [36,37]. Boundary asperity interaction would both form the oxide species through flash temperature increase but subsequently cause removal once the transient pressure conditions exceeded the durability of the film. Whilst this was similar to the mechanism suggested by Cutiongco and Chung [37], the effect of dynamic pressure on critical failure temperature was less distinct in the present work, with the influence of flash temperature increases perhaps masked by the external heating rate. Transient formation, removal and re-formation of the oxide layer may in itself be responsible for the low friction nature of the layer formed prior to scuffing as glaze layers typically require sufficient comminution of wear debris, however such a drop in the friction force during other reciprocating cast iron scuffing studies has not always been observed [9,11,14,38] and may be due to the differences in scuffing methodology (e.g. starvation, ramped load).

As mentioned above, the scanning electron microscopy image and corresponding EDX trace confirming both the presence of an iron oxide, but also its nanoscale morphology, which was similar to that observed by Saeidi et al. [14] in starved lubrication reciprocating scuffing studies of graphitic cast iron against a steel counter surface. Such a comminuted and compacted nanoscale structure was similar to high temperature 'glaze' layers observed across a number of different alloy systems [35,39,40]. These layers offer low friction coefficients but are often less durable as a form of wear protection, necessarily consuming the substrate material in order to form and only doing so within a range of elevated temperatures.

4.3. Scuffing sequence

Despite the difference in contact pressures between the two types of specimen surfaces, it was interesting to note that severe scuffing initiated at similar temperatures. This perhaps aligns with Blok's generic critical temperature theory [41] rather than Dyson's inlet entrainment model [42] as the contact geometries exhibited distinctive fluid film behaviour as observed in Fig. 8. Despite transition to the boundary lubrication condition and even in the absence of any chemical additives, the rate determining step of severe scuffing initiation appeared to be controlled by lubricant desorption, as an increase in the local contact pressure from the variable pressure specimen did not appear to have a significant impact on the initiation temperature. This was consistent with Bowman and Stachowiak [33] reflection that scuffing is intrinsically thermal in nature but also Quinn's narrative on oxidational wear [43] where once the desorption temperature of the lubricant is surpassed at an incipient scuffing site, protection from asperity induced oxide formation is limited at temperatures below 300 °C for ferrous materials.

It was clear that once lubricant desorption was complete below 250 °C scuffing would initiate, however initiation was clearly different between the respective samples. Oxide formation and scuffing damage appeared evenly distributed across the constant pressure sample, Fig. 9d). Even when the variable pressure sliding was terminated a few seconds after material transfer had accumulated to the counter surface, key scuffing initiation phenomena (oxide layer formation, disappearance of grinding marks [7,8]) could be observed in the area of highest contact pressure, although the oxide in this region exhibiting a similar average surface roughness compared to the constant pressure specimen despite the clear differences in wear morphology exhibited in Fig. 9. Thus differences in contact pressure experienced by the ring pack and piston skirt on the thrust side of the cylinder liner during the expansion stroke are perhaps secondary to effective liner lubrication in terms of severe scuffing initiation.

Consistent with the discussion on glaze layers above, such a low friction interface was transient in nature and not durable enough to resist the irreversible transition following severe scuffing initiation. The sequence of tribological events represented by this investigation can thus be summarised as follows: 1) Fluid film sliding at ambient conditions; 2) Transition to boundary sliding upon heating; 3) Formation of oxide species above 150 °C; 4) Formation of compacted low friction nanoscale oxide glaze layer prior to scuffing; 5) Removal of glaze and initiation of severe scuffing; 6) Severe accumulating adhesive wear between surfaces. Once the lubricant film desorbed due to the temperature increase, the coefficient of friction was influenced by the formation of surface oxide species prior to their subsequent removal that caused transition to severe scuffing.

5. Conclusions

- Variable pressure sliding of the top compression ring-liner contact in a heavy-duty diesel was successfully replicated on a bench tribometer by using numerical modelling to determine the required specimen geometry for a given contact load.
- The geometry of the variable pressure surface caused asymmetry in lubricant film formation according to the relative sliding direction due to both squeeze film effects and drip fed lubricant replenishment at the low pressure reversal position.
- The onset of severe scuffing in the present study was found to be independent of the applied contact pressure but dependent upon the interfacial temperature.
- At elevated temperatures the friction behaviour was influenced by the formation of a low friction oxide layer on the cast iron surface. Comminution of oxide debris led to very low (0.03) coefficient of friction values immediately prior to scuffing but the layer was unable to prevent severe adhesive wear once removed.

Declaration of Competing Interest

The authors declare that they have no known competing financial interests or personal relationships that could have appeared to influence the work reported in this paper.

Data availability

The authors are unable or have chosen not to specify which data has been used.

Acknowledgements

The authors would like to thank Ricardo for access to the RINKPAK suite of numerical modelling software. This research did not receive any specific grant from funding agencies in the public, commercial, or not-for-profit sectors. For the purpose of open access, the author has applied a CC BY public copyright licence to any Author Accepted Manuscript version arising from this submission.

Appendix of numerical parameters

Component parameters

		Bore	Piston	Top Ring	2nd Ring	Oil Ring
Material		FGI Cast iron	High alloy steel	17% Stainless	SGI Cast iron	17% Stainless
Diameter (mm)		132	132	132	132	132
Length (mm)		267	113.5			
Thickness (mm)		3.72		4.74	5.28	4.63
Width (mm)				2.4	2.36	3.32
Honing	Groove width (m)	2.237e-5				
	Depth (m)	3.5e-6				
	Density (1/m)	3946				
	Angle (deg)	51.9				
RMS Surface Height (m)		1e-7	1e-6	5e-7	6e-7	6e-7
Radius of curvature (m)		0.001	0.005	5e-5	0.0005	0.0005
Asperity density ($1/m^2$)		4e7	4e7	4e7	4e7	4e7
Young's Modulus (N/m^2)		1.7e11	1.8e11	1.8e11	1.7e11	1.8e11
Hardness (BHN)		180	169	123	170	123
Thermal expansion coefficient (1/K)		1.08e-5	1.24e-5	1.14e-5	1.14e-5	1.14e-5
Heat capacity (J/m^3 *K)		3656500		4000000	3592000	4000000
Thermal conductivity (W/m*K)		36.2		16.2	32.3	16.2
Heat transfer coefficient (W/m^2 *K)		3000				
Ring	Mass (kg)			0.041	0.029	0.040
	Tension (N)			43.2	30.41	51.1
	End gap (mm)			0.55	0.80	0.5
	Keystone angles (deg)			3.1, − 3.3	0	0

Friction parameters

Component Interface	Estimated Average Friction Coefficient
Piston crown – Cylinder bore	0.12
Piston crown – Piston pin	0.08
Top compression ring – Cylinder bore	0.21
Top compression ring – Ring groove	0.12
Second compression ring – Cylinder bore	0.08
Second compression ring – Ring groove	0.12
Oil control ring – Cylinder bore (Upper & lower)	0.21
Oil control ring – Ring groove (Upper & lower)	0.12
Connection rod – Piston pin	0.08
Piston skirt – Cylinder bore	0.12

Piston geometry parameters

Top groove width (mm)	3.6
Top groove depth (mm)	4.94
Second groove width (mm)	2.56
Second groove depth (mm)	3.57
Oil groove width (mm)	3.52
Oil groove depth (mm)	4.83
Land 1 top (mm)	0
Land 1 bottom (mm)	10
Land 2 top (mm)	13.6
Land 2 bottom (mm)	18.95
Land 3 top (mm)	21.51
Land 3 bottom (mm)	25.11
Land 4 top (mm)	28.63
Land 4 bottom (height) (mm)	113.5
Top crown to centre pin bore (mm)	74.07
Connecting Rod Length (mm)	268
Stroke Length (mm)	156
Pin length (mm)	88
Pin OD (mm)	58
Pin ID (mm)	23

Temperature Profile

Bore Axial Position (m)	Temperature (K)	Piston Land	Temperature (K)
0	475	1	500
0.028	430	2	430
0.0845	415	3	395
0.176	395	4	385
0.325	375		
Water jacket	378		

Lubricant properties

Oil type	SAE10W
Density (kg/m^3)	877
Heat capacity (J/m^3 *K)	1900,000
Thermal conductivity (W/m*K)	0.68
Cavitation Pressure (Pa)	99,990
Bulk modulus (Pa)	5e9
Piezo-viscosity coefficient (1/Pa)	1.1e-8
Pressure-viscosity index	0.67
Surface tension (N/m)	0.024

References

[1] ASTM A. Standard Terminology Relating to Wear and Erosion. G40, 2013.
[2] Barber G, Ludema KC. The break-in stage of cylinder-ring wear: a correlation between fired engines and a laboratory simulator. Wear 1987;118:57–75.
[3] Rahnejat H. Tribology and Dynamics of Engine and Powertrain: Fundamentals, Applications and Future Trends. Elsevier,; 2010.
[4] Qu J, Truhan JJ, Blau PJ. Investigation of the scuffing characteristics of candidate materials for heavy duty diesel fuel injectors. Tribol Int 2005;38:381–90.
[5] Booth J, Harvey T, Wood R, Powrie H. Scuffing detection of TU3 cam–follower contacts by electrostatic charge condition monitoring. Tribology Int 2010;43:113–28.
[6] Tasbaz O, Wood R, Browne M, Powrie H, Denuault G. Electrostatic monitoring of oil lubricated sliding point contacts for early detection of scuffing. Wear 1999;230:86–97.
[7] Kamps T, Walker J, Wood R, Lee P, Plint A. Reproducing automotive engine scuffing using a lubricated reciprocating contact. Wear 2015;332:1193–9.
[8] Kamps T, Walker J, Wood R, Lee P, Plint A. Scuffing mechanisms of EN-GJS 400-15 spheroidal graphite cast iron against a 52100 bearing steel in a PAO lubricated reciprocating contact. Wear 2017;376:1542–51.
[9] Olander P, Jacobson S. Scuffing resistance testing of piston ring materials for marine two-stroke diesel engines and mapping of the operating mechanisms. Wear 2015;330–331:42–8.
[10] Ajayi O, Lorenzo-Martin C, Erck R, Fenske G. Scuffing mechanism of near-surface material during lubricated severe sliding contact. Wear 2011;271:1750–3.
[11] Han J, Zhang R, Ajayi O, Barber G, Zou Q, Guessous L, et al. Scuffing behavior of gray iron and 1080 steel in reciprocating and rotational sliding. Wear 2011;271:1854–61.
[12] Wan S, Li D, Tieu AK, Zhang B. Comparison of the scuffing behaviour and wear resistance of candidate engineered coatings for automotive piston rings. Tribology Int 2017;106:10–22.
[13] Ma S, Chen W, Li C, Jin M, Huang R, Xu J. Wear Properties and Scuffing Resistance of the Cr–Al2O3 Coated Piston Rings: The Effect of Convexity Position on Barrel Surface. J Tribology 2019;141:021301.
[14] Saeidi F, Taylor A, Meylan B, Hoffmann P, Wasmer K. Origin of scuffing in grey cast iron-steel tribo-system. Mater Des 2017;116:622–30.
[15] Li W, Yu B, Ye B, Shen Y, Huang R, Du F. Effects of Cast-Iron Surface Texturing on the Anti-Scuffing Performance under Starved Lubrication. Materials 2019;12:1586.
[16] El-Sherbiny M. Cylinder liner wear. Tribology of Reciprocating Engines: Proceedings of the 9th Leeds–Lyon Symposium on Tribology Held in Bondington Hall, the University of Leeds, England 7–10 September 1982: Elsevier; 2017. p. 132.
[17] Plint A. The use of novel specimen designs in reciprocating line contact tests. STLE Annual Meeting. Atlanta, GA: STLE 2017.
[18] Carden P., Pisani C., Lainé E., Field I., Devine M., Schoeni A., et al. Calculation of crank train friction in a heavy duty truck engine and comparison with measured data. Proceedings of the Institution of Mechanical Engineers, Part J: Journal of Engineering Tribology. 2013;227:168–84.
[19] Xin Q. Diesel Engine System Design. Elsevier,; 2011.
[20] Gulwadi SD. Analysis of Tribological Performance of a Piston Ring Pack. Tribology Trans 2000;43:151–62.

[21] Reinhart T.E. Commercial medium-and heavy-duty truck fuel efficiency technology study-Report# 1. Washington, DC: National Highway Traffic Safety Administration.; 2015.
[22] Delprete C, Selmani E, Bisha A. Gas escape to crankcase: impact of system parameters on sealing behavior of a piston cylinder ring pack. Int J Energy Environ Eng 2019;10:207–20.
[23] Gravante S., Fenske G., Demas N., Erck R. Methods to Measure, Predict and Relate Friction, Wear and Fuel Economy. Ricardo Ltd., Shoreham-by-Sea (United Kingdom); Argonne National Lab.(ANL …; 2018.
[24] Truhan JJ, Qu J, Blau PJ. A rig test to measure friction and wear of heavy duty diesel engine piston rings and cylinder liners using realistic lubricants. Tribology Int 2005;38:211–8.
[25] Priest M, Taylor RI, Dowson D, Taylor CM. Boundary Conditions for Reynolds Equation with Particular Reference to Piston Ring Lubrication. In: Dowson D, Taylor CM, Childs THC, Dalmaz G, Berthier Y, Flamand L, et al., editors. Tribology Series. Elsevier; 1996. p. 441–52.
[26] Priest M., Dowson D., Taylor C.M. Theoretical modelling of cavitation in piston ring lubrication. Proceedings of the Institution of Mechanical Engineers, Part C: Journal of Mechanical Engineering Science. 2000;214:435–47.
[27] Johansson S, Nilsson PH, Ohlsson R, Rosén B-G. Experimental friction evaluation of cylinder liner/piston ring contact. Wear 2011;271:625–33.
[28] Priest M, Taylor CM. Automobile engine tribology—approaching the surface. Wear 2000;241:193–203.
[29] Guo L, Wang W, Zhang ZM, Wong PL. Study on the free edge effect on finite line contact elastohydrodynamic lubrication. Tribology Int 2017;116:482–90.
[30] Stejskal E., Cameron A. Optical interferometry study of film formation in lubrication of sliding and/or rolling contacts, 1972.
[31] Costa HL, Hutchings IM. Hydrodynamic lubrication of textured steel surfaces under reciprocating sliding conditions. Tribology Int 2007;40:1227–38.
[32] Taylor R. Squeeze film lubrication in piston rings and reciprocating contacts. Proceedings of the Institution of Mechanical Engineers, Part J: Journal of Engineering Tribology, 2015;229:977–88.
[33] Bowman W, Stachowiak G. A review of scuffing models. Tribol Lett 1996;2:113–31.
[34] Hsu S, Shen M, Klaus E, Cheng H, Lacey P. Mechano-chemical model: reaction temperatures in a concentrated contact. Wear 1994;175:209–18.
[35] Stott FH. High-temperature sliding wear of metals. Tribol Int 2002;35:489–95.
[36] Yoon H, Zhang J, Kelley F. Scuffing Characteristics of SAE 50B38 Steel Under Lubricated Conditions. Tribol Trans 2002;45:246–52.
[37] Cutiongco EC, Chung Y-W. Prediction of Scuffing Failure Based on Competitive Kinetics of Oxide Formation and Removal: Application to Lubricated Sliding of AISI 52100 Steel on Steel. Tribol Trans 1994;37:622–8.
[38] Tas MO, Banerji A, Lou M, Lukitsch MJ, Alpas AT. Roles of mirror-like surface finish and DLC coated piston rings on increasing scuffing resistance of cast iron cylinder liners. Wear 2017;376–377:1558–69.
[39] Walker J, Ross I, Reinhard C, Rainforth W, Hovsepian PE. High temperature tribological performance of CrAlYN/CrN nanoscale multilayer coatings deposited on γ-TiAl. Wear 2009;267:965–75.
[40] Jiang J, Stott F, Stack M. A generic model for dry sliding wear of metals at elevated temperatures. Wear 2004;256:973–85.
[41] Blok H. The postulate about the constancy of scoring temperature. NASA Spec Publ 1970;237:153.
[42] Dyson A. The Failure of Elastohydrodynamic Lubrication of Circumferentially Ground Discs. Proceedings of the Institution of Mechanical Engineers, 1976;190:699–711.
[43] Quinn TFJ. Review of oxidational wear: Part I: The origins of oxidational wear. Tribol Int 1983;16:257–71.